Article:
Wei, Z., Huang, Y., Wignall, P.B. et al. (2026) Endolithic bloom linking with volcanic activities and biocrisis at the onset of the Guadalupian–Lopingian (Permian) extinction. Global and Planetary Change, 262. 105438. ISSN: 0921-8181

https://doi.org/10.1016/j.gloplacha.2026.105438

Endolithic bloom linking with volcanic activities and biocrisis at the onset of the Guadalupian–Lopingian (Permian) extinction

Zhensheng Wei [1], Yuangeng Huang [1], Paul B. Wignall [2], Pieter T. Visscher [1,3], Qian Fang [1], Xincheng Qiu [1], Danna Liu [1], Zijie Zheng [1], Xueqian Feng [1], Zhong-Qiang Chen [1, *]

[1] State Key Laboratory of Geomicrobiology and Environmental Changes, China University of Geosciences (Wuhan), Wuhan 430074, China

[2] School of Earth and Environment, University of Leeds, Leeds LS2 9JT, UK

[3] Department of Marine Sciences, University of Connecticut, 1080 Shennecossett Road, Groton, CT 06340, USA

Corresponding author: Zhong-Qiang Chen (zhong.qiang.chen@cug.edu.cn)

ABSTRACT

Large-scale volcanism has been implicated in causing Phanerozoic mass extinctions, but little direct evidence of the effects of volcanism on microbiota interaction exist. Here we report abundant endolithic microboring traces from the Guadalupian–Lopingian (G–L; Permian) mass extinction transition in South China. Microanalyses using scanning electron microscopy (SEM), Raman spectroscopy, and nanoscale secondary ion mass spectrometry (NanoSIMS) reveal microborings

comprising organic carbon, anatase, calcite, quartz, and clay minerals. Large amounts of organic carbon exhibit Raman spectrum peaks at ~1366 cm^{-1} and ~1603 cm^{-1}, along with intense signals of $^{12}C^-$ and $^{12}C^{14}N^-$ in NanoSIMS ion maps are interpreted as remnants of endolithic organisms or residues of their metabolic products. Well-crystallized quartz crystals, which can be assigned to α-quartz of volcanic provenance, are regularly aligned along microboring margins, reinforced by strong signals of $^{28}Si^+$ in NanoSIMS ion maps, suggesting that microbial adsorption of volcanic material during endolithic activity. Stratigraphic peak abundances of microborings and microbiota coincide with initial eruption phase of the Emeishan volcanism, implying that volcanic activity may have stimulated an endolithic bloom at the onset of the G-L mass extinction.

Keywords: Guadalupian–Lopingian mass extinction, microboring, Emeishan Large Igneous Province, South China

1. Introduction

Volatile volcanism has been proposed as a trigger of the Ordovician–Silurian, Frasnian–Famennian, Guadalupian-Lopingian (G–L), Permian–Triassic, and Triassic–Jurassic mass extinctions (Svensen et al., 2009; Bond and Grasby, 2017; Burgess et al., 2017; Grasby et al., 2017; Clapham and Renne, 2019; Racki, 2020; Li

et al., 2024). In addition, volcanic activity has been proposed as a critical driver of a phased benthic faunal community and microfauna restructuring during various intervals (Waśkowska, 2011; Perrier et al., 2012; Punekar et al., 2014). Despite extensive studies on the impact of volcanism on heterotrophic macrofaunal and microfaunal assemblages, the response of microboring organisms (mainly autotrophic phytoplankton excepting for some heterotrophic fungi) to such an event remain overlooked, and records of their reactions to volcanic eruptions are sparse.

In modern oceans, inputs from volcanic activities can promote planktonic communities and thus influencing biogeochemical cycles, not only via macronutrients but also through limiting micronutrients (e.g., iron and manganese) supplied by volcanic ash, tephra, especially subaerial volcanism (Duggen et al., 2010; Langmann et al., 2010; Zhang et al., 2017; Li et al., 2020; Longman et al., 2022; Bisson et al., 2023). While these are well documented in the present-day ocean, however, such interactions are rarely preserved in deep-time stratigraphy, particularly during biotic crises.

The G–L transition was marked by major biodiversity losses of benthic groups and collapse of metazoan reefs in South China (Jin et al., 1994a; Stanley and Yang, 1994; Shen and Shi, 2002; Wang et al., 2004; Kaiho et al., 2005; Clapham et al., 2009; Chen et al., 2009; Wignall et al., 2009; Huang et al., 2019a; Song et al., 2023; Li et al., 2024). The Hg anomalies in strata near the G–L boundary of the Global Stratotype Section and Point (GSSP) at Penglaitan (PLT) in the Laibin region of South China (Fig. 1B), revealed that the volatile eruption of the Emeishan Large Igneous Province

(ELIP) coincided with a biotic crisis (Huang et al., 2019a, 2022; Kaiho et al., 2023). Microbiota developed in abundance after the collapse of the sponge-bryozoan reef at onset of the G–L mass extinction. Nevertheless, no direct evidence of the interaction of volcanism and microbiota over the G–L transition has been reported (Huang et al., 2019a).

Based on preliminary studies of the microbiota during this period by Huang et al., 2019a, here we report profuse endolithic microborings presumably produced by cyanobacteria and chlorophytes (Golubic et al., 1975) from the G–L boundary beds at the Penglaitan section (Fig. 1). High-precision, *in-situ* microanalyses probed the volcanic residues filling in microborings. Combined with the stratigraphic distribution of these microborings, this study provides direct evidence of volcanic activities linked with a microbial proliferation at the onset of the G–L extinction.

2. Geological setting

During the G–L transition, South China was situated at equator latitudes in eastern Paleo-Tethys Ocean (Fig. 1A; Gao et al., 2025; Win et al., 2025), and the Laibin area was located in the eastern Dianqiangui Basin, the southwestern margin of the South China Block (Feng et al., 1994; Chen et al., 1998; Wang and Jin, 2000; Jin et al., 2006). Since the Devonian, the Dianqiangui Basin has experienced repeated tectonic activity and syn-sedimentary faulting, resulting in alternating platform-basin depositional systems (Feng et al., 1994; Chen et al., 1998; Wang and Jin, 2000). The Laibin area represents the ramp settings between carbonate platforms located to the

west and north (Heshan area) and the deep-water Qingzhou Trough to the southeast (Jin et al., 1994b, 2006; Shen et al., 2007). The development of the ELIP during the middle-late Permian led to extensive basaltic volcanism, lithospheric thinning, and regional crustal uplift (He et al., 2003, 2007; Xu et al., 2004). These volcanism-induced tectonic activities profoundly modified the paleogeographic settings of South China, causing widespread regression, enhanced erosion of uplifted areas, and major facies changes across the Dianqiangui Basin (Chen et al., 1998, 2009; Jin et al., 2006; Mei et al., 2007).

Moreover, the largest regression in the Phanerozoic, coinciding with the Dongwu uplift in China (Feng et al., 1994), occurred in the middle-late Permian transition (Jin et al., 1994b, 2006; Chen et al., 1998, 2009; Haq and Shutter, 2008; Lucas and Shen, 2018), resulting in a widespread distinct disconformity in most areas around the world, particularly in the shallow platform settings. Only a few areas, such as central part of South China, Central Iran, and southeastern Pamir were relatively low and recorded continuous successions across the G–L boundary (Lucas and Shen, 2018). In central South China, the complete middle-late Permian successions are well exposed at the Tieqiao and Penglaitan sections of the Laibin area, Guangxi Province. These two sections although ~10 km apart both record comparable successions along the western and eastern limbs of a large syncline (Fig. 1; Jin et al., 2006; Shen et al., 2007; Huang et al., 2019b).

The GSSP for the Guadalupian-Lopingian (Permian) was nominated at the Penglaitan section (Jin et al., 2006), which is situated ~20 km of Laibin, central

Guangxi Province, South China (Fig. 1B and C). The G–L boundary strata at Penglaitan comprise seven beds. Beds 1–6 comprise limestones and are assigned to the Maokou Formation, while Bed 7 is dominated by siliceous mudstone of the basal Heshan Formation. Of these, Bed 4 is a sponge-bryozoan reef. The G–L boundary was placed at the base of Bed 6k by the first appearance datum (FAD) of conodont *Clarkina postbitteri postbitteri* (Jin et al., 2006). Recently, Shen et al. (2023) redefined the GSSP for the G–L boundary and moved the boundary to the base of Bed 6j, using the FAD of conodont *C. postbitteri* at Penglaitan. Detailed section and lithologic descriptions have been given in previous studies (Jin et al., 2006; Wignall et al., 2009; Huang et al., 2019a; Shen et al., 2023).

3. Material and methods

3.1. Quantitative analyses for microborings and quartz crystals

A total of 143 petrographic thin sections prepared from samples of Beds 2a to 7i in PLT section were used for identification and statistical analyses of the frequency of microborings using optical and fluorescence microscopy at the State Key Laboratory of Geomicrobiology and Environmental Changes (GMEC), China University of Geosciences (CUG) at Wuhan, China. Thin sections that were investigated covered Beds 2a–7i, and averagely two thin sections (each 3 × 2.5 cm in size) were observed from each sample. We documented microboring counts (MC) and microboring

densities (MD) in a single microscopic view to describe the number of microborings and the percentage of area occupied by microborings within the entire area of the view, respectively (Chen et al., 2009). The field of view was subdivided into numerous grids, and microboring and host areas in each grid were measured and their ratios were calculated, after which the MDs in all views of the entire sample was calculated.

We employed quartz abundance (QA) to record the approximate content of this mineral in one sample based on the amount quartz-grain cover with scanning electronic microscopy (SEM; see below). Quartz grains derived from volcanic ash were identified based on their euhedral to subhedral crystal forms (bipyramidal and euhedral pseudo-hexagonal crystals) and low roundness. In contrast, detrital quartz typically exhibits rounded to subrounded outlines and mechanical surface features such as percussion dents or amorphous silicon overgrowths (Fisher and Schmincke, 1984; Madhavaraju et al., 2006; Symth et al., 2008; Wu et al., 2017; Itamiya et al., 2019; Pei et al., 2019). Samples covered Beds 4a–7a, and averagely 4 cm^2 were observed from each sample. Note that QA is not the same as the amount of quartz in the microfacies because it is difficult to count the number of quartz-grains accurately. Any single area of view may either have a very large number of quartz-grains (e.g. Bed 6a and 6c), or only a few (e.g. Bed 6h and 6k). No quartz-grains or crystals were found in the matrix of any of the limestone samples from the G–L succession at Penglaitan.

155 *3.2. Micro-analyses using SEM and Raman spectrum*

156

157 Freshly broken up rock samples were rinsed for approximately 3s in 10% acetic
158 acid and washed for 15s to remove residual acid using dionized water. The samples
159 were then inspected for the presence of microbial fossils under a HITACHI SU8010
160 field emission scanning electronic microscope (FESEM) [at GMEC] after surface
161 spraying of platinum for 2 minutes. The voltage used when observing the sample is
162 15kV, and the current is 10 μA. When using EDS for elemental distribution mapping,
163 these two values will be increased to 25kV and 15 μA to obtain a stronger signal (Liu
164 et al., 2024).

165 Raman spectra were acquired with confocal micro-Raman spectroscopy with
166 rapid analysis using a WITec Alpha 300-R at BGEG, which is non-destructive for the
167 sample. The instrument was equipped with a 532-nm wavelength laser set at a power
168 level of 5mW. The integration time was 1–10s per point and the accumulation number
169 was 1–10 times, and for mineral mapping, 2s per point and 1 time accumulation was
170 used. This approach is required for mapping, which involves performing thousands of
171 point analyses in a defined area in a systematic manner. Extended continuous analyses,
172 however, increases the risk of instrument failure. Moreover, before conducting the
173 mapping, we performed point analyses using the same parameters to ensure adequate
174 signal strength. The mapping results therefore are reliable.

175

176 *3.3. Ion mapping using NanoSIMS*

Ion maps of carbon ($^{12}C^-$), nitrogen (measured as $^{12}C^{14}N^-$), sulfur ($^{32}S^-$), phosphorus ($^{31}P^{16}O^-$), and silicon ($^{28}Si^+$) were produced using a Cameca NanoSIMS 50L [at GMEC]. NanoSIMS is an *in-situ* and nearly non-destructive microanalysis technique. The primary ion beam with thousands of volts bombards the sample surface and causes ionized atoms and small molecules (i.e. secondary ions) on the upper layers of sample, which are physically separated and counted in the mass spectrometer (Hoppe et al., 2013). This technology is used to detect the ion abundance of the life-essential elements, such as carbon, nitrogen, and sulfur, which has been applied to characterize microorganism fossils from the Precambrian strata (Oehler et al., 2009; Wacey et al., 2011; Peng et al., 2016; Guo et al., 2018; Qiu et al., 2025). Thin sections polished into 1 cm diameter discs served as samples for analysis. A focused primary beam of $^{133}Cs^+$ ions produced secondary ions from the sample surface. Prior to formal analyses, we performed approximately 5 minutes of pre-sputtering onto the sample surface to remove potential surface contaminants and enhance the signal quality during subsequent analysis. The total time of analysis of a single sample was about 25 min. Since samples were non-conductive, the electron gun was activated during measurements to neutralize the positive charge deposition caused by the primary beam and to minimize the effects of surface charging. Custom software, WinImage (from Cameca), was used to process data and generate images.

4. Results

199

200 *4.1. Morphology of microborings*

201

202 Microborings were abundant in the G–L succession in Penglaitan, and mostly
203 occurred within bioclasts (Fig. 2A–D). Host taxa of these borings included
204 brachiopods, trilobites, crinoids, bryozoans, corals and unclassified *Tubiphytes*. All
205 microborings showed strong fluorescence under microscopy (Fig. 2B) and could be
206 assigned to three morphologic categories: nodular, radial, and filamentous (Figs.
207 2A–2D, 3). The first type appeared as dense networks of dichotomous branching
208 filaments. The individual filaments were strip-shaped, slightly curved to straight, and
209 40–200 μm long, with distinct nodular swellings (20–30 μm in diameter) (Figs. 2A
210 and B, 3A–C). Filamentous microborings included flattened, oval swellings, < 10 μm
211 in diameter, with simple (i.e., non-branching) filaments from tens to hundreds μm in
212 length (Figs. 2C, 3G–I). These microborings occasionally possess fewer branches, and
213 individuals from different layers cross-cut and overlap, creating the illusion of a
214 network-like structure on host substrate. Radial microborings comprised rounded,
215 clustered swellings, 25–35 μm in diameter, without filaments or columnar bifurcated
216 filaments, (Figs. 2d, 3D–F). The microborings and substrates were composed of
217 microcrystalline calcite, and recrystallized sparry calcite was not observed (Fig. 4A
218 and B).

219 SEM imaging revealed that outline of microborings were usually strip- or
220 tube-shaped, occasionally branched in longitudinal sections (Fig. 2E and F), and were

221 radial or irregular in transverse section. Tubular microborings truncated the original
222 texture of hosting shell (Figs. 2E and F, 4). About 85% and 15% of the microborings
223 were oriented parallel and perpendicular to the alignments shown by the shell texture,
224 respectively.
225
226 *4.2. Mineral, elemental and isotopic compositions infillings*
227
228 SEM imaging showed that microboring infillings comprised quartz and clay minerals.
229 The central clay minerals were typically interlayered with discrete quartz crystal
230 layers and bordered externally by brachiopod shell fragments, forming a distinct
231 clay-quartz-shell tripartite sequence (Figs. 2E–H, 4C and D). The quartz crystals were
232 distributed along microboring margins in cross section (Fig. 2G and H), with a small
233 amount scattering in the core of microboring. A few crystals were occasionally
234 observed on the surface of the non-boring part of the same hosting shell, where these
235 crystals slightly truncated the outer layers of the brachiopod shell (Fig. 2I–L). No
236 quartz crystals were observed in the matrix of any of the limestone samples from the
237 G–L succession of Penglaitan either under optical microscopy or SEM.
238 The EDS elemental mapping exhibited strong signals of Si, O, Al, K, and Ti in
239 infillings (Fig. 5A), while Ca signal was very strong in host shell. Si concentrated
240 along microboring margins, with a small amount in the core of infilling, and almost
241 no signal of Si occurred in host shell. Ca, C and O all were present in both infillings
242 and host shells, but both Ca and C signals are distinct in hosting shell and O is

243 stronger in fillings than that in hosting shells (Fig. 5A). Elemental mapping
244 observations are corroborated by point analysis of EDS in which Si, Ca, O, Al, K, and
245 Ti signals are rather strong, and the signal of Fe weak (Fig. 6).
246 Raman spectroscopy spectra (Fig. 5B and C) showed peaks of organic carbon
247 (~1366 cm^{-1} and ~1603 cm^{-1}, Fig. 5G). In addition to organic carbon, the result
248 revealed two minerals identified as anatase (at ~143, 395, 517, 638 cm^{-1}, Fig. 5F), and
249 calcite (~281 and 1088 cm^{-1}; Fig. 5E), respectively. The organic carbon and anatase
250 were associated with infillings, while calcite mostly occurred at microboring margins
251 and adjacent to host shells. Abundant quartz grains, with spectrum peak of ~466 cm^{-1}
252 were present along microboring edges (Fig. 5D).
253 NanoSIMS ion maps of $^{12}C^-$, $^{12}C^{14}N^-$, $^{32}S^-$, $^{28}Si^+$, and $^{31}P^{16}O^-$ along a transverse
254 section of a microboring displayed strong signals of $^{12}C^-$, $^{12}C^{14}N^-$, $^{32}S^-$, and $^{31}P^{16}O^-$ in
255 the core of infilling. In contrast, infilling margins yielded higher concentrations of $^{32}S^-$,
256 which signals were decoupled with the distribution of $^{12}C^-$ (Fig. 7A). A longitudinal
257 section of another microboring showed intense signals of both $^{12}C^-$ and $^{12}C^{14}N^-$
258 scattered throughout the infilling (Fig. 7B). The $^{12}C^-$-enriched area was typically
259 accompanied by a high intensity of $^{12}C^{14}N^-$, similar to the distribution of $^{32}S^-$, although
260 the latter had a weaker signal (Fig. 7B). Signals of $^{28}Si^+$ had a broader distribution
261 pattern than the isotopes of other elements within the microboring and were more
262 intense around microboring margins (Fig. 7B).
263
264 *4.3. Stratigraphic abundance and distribution of microborings and quartz grains*

In the Penglaitan section, microboring counts section increased from Bed 5a and peaked in Bed 6f, then steadily declined to Bed 6k (Fig. 8). Microboring density (MD) was low in Beds 4 and 5, with a maximum value in Bed 4k (capping the bryozoan-sponge reef). The MD increased in Bed 6, with maxima coinciding with high values of quartz abundance (Fig. 8). The highest MD was observed in Bed 6g–j. Only either coccoid-like spheroids or bacterial clump-like spheroids occurred in Bed 4–5b, both coccoid-like spheroids and bacterial clump-like spheroids in Bed 5c and all three types, coccoid-like spheroids, bacterial clump-like spheroids and *Ovummurus duoportius* (Huang et al. 2019a), were found in Bed 6a–k, indicating an upward increase of morphotype abundance (Fig. 8).

The quartz crystals were only present in Bed 6 and showed peak abundances in Bed 6a–c and Bed 6g–j. Quartz crystals were not observed in microborings from Beds 4–5 (Fig. 8), and were also absent in the matrix outside of the bioclasts in all thin sections of the G–L succession at Penglaitan that were investigated.

5. Discussion

5.1. Endolithic microorganisms

Although microborings occur in various benthic taxa, they are predominantly found associated with brachiopod shells (Figs. 2E and F, 3). Nodular, radial, and filamentous

287 microborings are morphologically similar to the microboring ichnotaxa: *Eurygonum*
288 *nodosum* Schmidt, 1992 (Huang et al., 2019a), *Fascichnus frutex* Radtke, 1991, and
289 *Ichnoreticulina elegans* Radtke, 1991, respectively. The latter two have been
290 re-described and illustrated by Wisshak et al. (2008). Vacuum-cast embedding is an
291 ideal approach for the taxonomic study of microboring. However, this method cannot
292 be applied to fossil microboring that have been filled in with sediments (Golubic et al.,
293 1970; Wisshak et al., 2008). Therefore, many studies resort to optical microscopy to
294 describe the characteristics of microborings but not assign to specific ichnotaxa
295 because of the limitations in two-dimensional visualization from three-dimensional
296 objects (Olóriz et al., 2004; Wisshak, 2012; Rifl et al., 2022). Notably, microborings
297 under petrographic thin sections typically preserve more informative data. For
298 example, variations in abundance morphological features of microborings provide
299 invaluable insights in the properties of the depositional environments (Olóriz et al.,
300 2004; Rifl et al., 2022). In addition, these materials also typically preserve
301 information about impregnation minerals, spar cement, and secondary mineralization
302 *in situ*, which can be employed for assessing the taphonomic process of endoliths
303 (Kołodziej et al., 2012).

304 The microboring records in our samples did not show significant calcite
305 recrystallization, blocky cementation, or fabric-disruptive dolomitization (Fig. 4),
306 indicating that the microborings have been minimally affected by later diagenetic
307 alteration and retained their original geochemical signals. In our study, Raman
308 spectrum clearly shows the abundance of organic matter within microborings (Fig. 5C

and G). This observation is substantiated by co-occurrence of distinct $^{12}C^-$ and $^{12}C^{14}N^-$ patterns using NanoSIMS ion mapping (Fig. 5A and B) (Oehler et al., 2009; Wacey et al., 2011; Peng et al., 2016; Trembath-Reichert et al. 2021). The intense signal of $^{31}P^{16}O^-$ and moderate distribution of $^{32}S^-$ further strengthen the presence of organic carbon in microborings (Fig. 7A and B). The presence of these ions typically indicates microbial activity, particularly $^{12}C^{14}N^-$ and $^{31}P^{16}O^-$, which are commonly found in the residual cell walls/sheaths of microfossils rather than surrounding rocks (Peng et al., 2016). The $^{32}S^-$ may originate from microbial preservation processes or could be introduced during early diagenesis (Werne et al., 2000). We also ruled out that sulfur was incorporated by sedimentary processes and mineralization alteration since pyrite was rather rare in our samples. These results demonstrate that organic matter could represent remnants of endolithic microorganisms or residues of their metabolic products, which would imply that endolithic microorganism produced the microborings.

5.2. Interactions between endolithic microorganism and volcanic products

Quartz crystals were absent in the limestone matrix of the G–L succession, but were commonly associated with microborings in brachiopod shells (Figs. 2E and H, 5A, 7A and B) and occasionally on non-bored shell surface (Fig. 2G–L). Authigenic quartz crystals with blocky morphology likely formed within brachiopod shells during early diagenesis (Schmitt and Boyd, 1981). These quartz inclusions mimic the fibrous

structure of brachiopod skeletal carbonates, as silicate-rich pore fluids could precipitate rapidly, replacing fine structures upon calcite dissolution (Maliva and Siever, 1988; Schmitt and Boyd, 1981). Microbially-induced authigenic quartz precipitates typically exhibit ordered alignment with minimal surface abrasion and are often associated with iron-bearing illites (Luo et al., 2016), which were not observed here. Instead, well-crystallized quartz was found within microborings and on shell surfaces in Bed 6a–k (Fig. 2). The quartz displays hexagonal, bipyramidal, or combined morphologies (Fig. 2G–H, K–L), consistent with α-quartz (a polymorph), which is stable at low surface temperatures (<573°C), suggesting a volcanic provenance (Smyth et al., 2008).

Except for quartz, microborings contain anatase and authigenic titanium oxide particles (Fig. 5A and B). Anatase may form through (1) diagenetic alteration, (2) detrital release from clay minerals, or (3) *in situ* authigenic precipitation (Weibel and Friis, 2004). During early diagenesis, Ti ions can complex with organic ligands on cell surfaces or exopolymeric matrices (Galvezetal et al., 2012). Subsequent alteration releases Ti, which precipitates as anatase, implying organic matter adsorption (Sirantoine et al., 2021). However, Raman spectroscopy (Fig. 5F and G) reveals that dispersed organic matter within microboring (Fig. 5M and N), indicating that anantase formation was not microbially mediated but rather derived from exogenous sources.

Cyanobacterial microborings in carbonate grains of Bahamian sediments showed rapid infilling by radial fibrous aragonite, indicating that the microboring activity and carbonate precipitation could occur almost simultaneously in carbonate depositional

353 environments (Reid and Macintyre, 2000). Penglaitan sediments share an analogous
354 carbonate environment, yet the microborings contain considerably less carbonate.
355 This could imply that volcanic minerals were actively agglutinated by endoliths rather
356 than passively deposited. Some endolithic microorganisms produce exopolymeric
357 substances (Golubic et al., 2000; Reid and Macintyre, 2000; Bonacolta et al., 2024)
358 that could bind fine material (Flemming et al., 2025), including volcanic ash. This
359 trapping mechanism could produce large aggregates composed of Si and Al-rich
360 granular or irregular fibrous and/or flaky minerals (Fang et al., 2017; Kawano and
361 Tomita, 2001). Thus, endolithic boring behavior could deposit organic-ash mineral
362 complexes similar to dissolution-precipitation activity in modern sediments
363 (Macintyre et al., 2000; Reid et al., 2000). Such a biogenic mechanism in our samples
364 is supported by an alignment of quartz crystals along the microborings (Fig. 2G and
365 H), which similarly to observation in contemporary carbonate systems would ensure
366 tunnel functionality during active boring. Despite volcanic quartz scarcity in
367 high-energy environment like packstones (Pei et al., 2019), our findings emphasize a
368 critical role of microbes in amalgamation of volcanic material.
369
370 *5.3. Endolithic bloom linking with volatile volcanism and biocrisis*
371
372 Our observations support that both microborings and quartz reach peak abundance in
373 Bed 6 (Fig. 8; Tables S1–S3 in Supplementary Information). The negative $\delta^{13}C_{carb}$
374 excursion and initial Hg/TOC peak in Bed 6a likely reflect the initial eruption or soot

deposition from volcanic heating associated with the ELIP (Huang et al., 2019a; Kaiho et al., 2023). Subsequent records show the most pronounced negative $\delta^{13}C_{carb}$ excursion coupled with elevated Hg/TOC ratios in Beds 6g and 7a, marking the main eruptive phase of ELIP volcanism (Huang et al., 2019a, 2022). In addition to geochemical records from the Penglaitan section, previous studies have confirmed that the ELIP experienced multiple episodes of volcanic activities and the earlier activity occurred prior to 260 Ma (He et al., 2007; Sun et al., 2010; Huang et al., 2016; Xiao et al., 2024; Zhao et al., 2025). The claystones between Beds 5 and 6 in Penglaitan section were derived from ELIP (Zhong et al., 2013). The integration of our new findings and previous studies indicates the synchroneity of microbiotal proliferation and volcanism just before the G–L mass extinction.

Such volcanic events typically induce marine eutrophication, temporarily enhancing marine primary productivity while ultimately expanding anoxic zones, a biogeochemical cascade that frequently precedes biocrises (Ernst and Youbi, 2017). While ELIP-derived nutrients may have initially stimulated endolithic proliferation, analogous to interactions between volcanic ash and microbes in modern oceans (Uematsu et al., 2004; Zhang et al., 2017), the resulting prolonged anoxia likely imposed metabolic limitations on these communities (Zhang et al., 2021). This sequence explains the stratigraphically resolved decline observed across the G–L boundary interval (Fig. 8). Notably, endolithic blooms undoubtedly predate the first Hg peak (Fig. 8) and were succeeded by diverse microbiota filled the vacated niche (Huang et al. 2019a), suggesting their role in metazoan reef collapse.

Previous studies showed that most of deep-time endolithic microborings destroyed predominantly relatively soluble material (e.g., carbonate or phosphate biogenic substances) such as shells or fragmented skeletons (Golubic et al., 1975). In the Penglaitan section, the majority of microborings presumably occurred on shell fragments of various taxa (Fig. 2A–D), irrespective of the host animals were alive or dead. Modern observation and fossil records show that some microborings occur in live stromatoporoids and corals, and are preserved within the hosts' accretional skeletal fabrics, because endolithic microbiota synchronize their colonization rate with the skeletal accretion rates of their hosts to sustain exposure to light, which is critical for their phototrophic survival (Le Campion-Alsumar et al., 1995; Kołodziej et al., 2012; Wu et al., 2013; Pernice et al., 2020). Although microboring and quartz crystal deposition occasionally occur on brachiopod shell surfaces, slightly truncating the outer fibrous layers (Fig. 2K and L), it is difficult to determine whether the hosts were alive when the erosion occurred. It is not possible to identify whether the changes in the shell fibrous structure are resulted from repair or diagenesis (Casella et al., 2018). Whether endolithic microorganisms drove the G–L extinction remains unclear, but they plausibly played a major role in the collapse of the metazoan reef (Fig. 8).

Microborings and benthic microbiota were absent in and above Bed 7, and we hypothesize that the disappearance of microboring was caused by the combined effects of the G–L mass extinction and depositional environmental change. The G–L extinction led to the widespread disappearance of calcareous benthic organisms (Bond

et al., 2010), depriving microborings of their fundamental preservation substrate. In addition, Bed 7 and above strata are comprised of cherty mudstone with interlayer of bioclastic limestone, indicative of a relatively deep offshore to basin setting (Chen et al., 2009; Wignall et al., 2009; Huang et al., 2019a; Fig. 8), where endoliths could not survive via photosynthesis. It should be noted that the disappearance of microborings did not indicate that the endoliths were suffered from G–L mass extinction, because similar fossil records were preserved in later geological periods (Glaub and Vogel, 2004).

Beds 5–6 are associated with shallow, agitated environments (Wignall et al., 2009). Such wave-active shallow zones favored phototrophic endolithic proliferation (Rifl et al., 2022). However, even in environments with persistently high-energy settings, microborings are typically discontinuous because only external drivers stimulate the microbial boring activity (e.g., tectonic activity and grazing) (Olóriz et al., 2004; Kołodziej et al., 2012). Mineral composition of microboring infillings combined with statistical analyses reveals coinciding shifts in volcanic geochemical proxies (e.g., Hg/TOC ratios, Fe, Cu). These analyses demonstrate a significant association between microboring activity and the ELIP, suggesting that volcanic forcing, rather than sea-level fluctuations, was the primary driver of endolithic blooms during the G–L transition. Based on the presented evidence, we propose that this proliferation represents a regional anomaly rather than a global stratigraphic signature. However, further validation from additional sections is required to confirm this hypothesis.

6. Conclusions

Abundant nodular, radial, and filamentous microboring traces are detected in skeletal fragments of various taxa associated with the G–L boundary beds in the Penglaitan section. Elemental, mineral and isotopic mappings of EDS, Raman spectrum and NanoSIMS reveal that microboring infillings comprised organic carbon, anatase, calcite, quartz, and other clay minerals. Organic carbon within microboring, indicated by intense signals of both $^{12}C^-$ and $^{12}C^{14}N^-$ are interpreted as remnants of endolithic microorganisms or residues of their metabolic products. Quartz grains are abundant within microborings, with additional few scattered on non-bored shells. These quartz crystals are usually tetragonal, hexagonal, and bipyramidal in outline, typical of α-quartz of volcanic provenance. Regular arrangement of quartz along microboring margins suggests that endolithic microorganisms were involved in the active sequestration of volcanic material. Stratigraphic peak abundances of microborings and microbiota coincide with the initial eruption of the ELIP indicated by Hg anomaly. This implies that volcanic ash inputs may have promoted microbial blooms at the onset of G–L extinction.

Declaration of Competing Interest

The authors declare that they have no known competing financial interests or personal

relationships that could have appeared to influence the work reported in this paper.

Acknowledgments

We thank Hongfei Chen, Zhemin Zheng, and Lewei Su for insistence in the field and Hao Yang for help in laboratory experiments. We are grateful to two anonymous reviewers for their constructive comments, which have greatly improved the quality of the manuscript. This study was supported by National Nature Science Foundation of China grants (42530209, 42302347) and Fundamental Research Funds for National Universities, China University of Geosciences (No. 2025XLA46).

Data Availability Statement

Data supporting the findings of this study are available in the Supporting Information of this article.

References

Bisson, K.M., Gassó, S., Mahowald, N., Wagner, S., Koffman, B., Carn, S.A., Deutsch, S., Gazel, E., Kramer, S., Krotkov, N., Mitchell, C., Pritchard, M.E., Stamieszkin, K., Wilson, C., 2023. Observing ocean ecosystem responses to volcanic ash. Remote Sens. Environ. 296, 113749.

Bonacolta, A.M., Visscher, P.T., del Campo, J., White III, R.A., 2024. The eukaryome of modern microbialites reveals distinct colonization across aquatic ecosystems. npj Biofilms Microbiomes 10, 1–11.

Bond, D.P.G., Grasby, S.E., 2017. On the causes of mass extinctions. Palaeogeogr. Palaeoclimatol. Palaeoecol. 478, 3–29.

Bond, D.P.G., Hilton, J., Wignall, P.B., Ali, J.R., Stevens, L.G., Sun, Y., Lai, X., 2010. The Middle Permian (Capitanian) mass extinction on land and in the oceans. Earth-Sci. Rev. 102, 100–116.

Burgess, S.D., Muirhead, J.D., Bowring, S.A., 2017. Initial pulse of Siberian Traps sills as the trigger of the end-Permian mass extinction. Nat. Communs. 8, 164.

Casella, L.A., Griesshaber, E., Simonet Roda, M., Ziegler, A., Mavromatis, V., Henkel, D., Laudien, J., Häussermann, V., Neuser, R.D., Angiolini, L., Dietzel, M., Eisenhauer, A., Immenhauser, A., Brand, U., Schmahl, W.W., 2018. Micro- and nanostructures reflect the degree of diagenetic alteration in modern and fossil brachiopod shell calcite: A multi-analytical screening approach (CL, FE-SEM, AFM, EBSD). Palaeogeogr. Palaeoclimatol. Palaeoecol. 502, 13–30.

Chen, Z.-Q., Jin, Y.G., Shi, G.R., 1998. Permian transgression-regression sequences and sea-level changes of South China. Proc. Roy. Soc. Victoria 110, 345–367.

Chen, Z.-Q., George, A.D., Yang, W.-R., 2009. Effects of Middle–Late Permian sea-level changes and mass extinction on the formation of the Tieqiao skeletal mound in the Laibin area, South China. Austr. J. Earth Sci. 56, 745–763.

505 Clapham, M.E., Shen, S., Bottjer, D.J., 2009. The double mass extinction revisited:
506 reassessing the severity, selectivity, and causes of the end-Guadalupian biotic
507 crisis (Late Permian). Paleobiology 35, 32–50.
508 Clapham, M.E., Renne, P.R., 2019. Flood basalts and mass extinctions. Ann. Rev.
509 Earth Planet. Sci. 47, 275–303.
510 Duggen, S., Olgun, N., Croot, P., Hoffmann, L., Dietze, H., Delmelle, P., Teschner, C.,
511 2010. The role of airborne volcanic ash for the surface ocean biogeochemical
512 iron-cycle: a review. Biogeosci. 7, 827–844.
513 Ernst, R.E., Youbi, N., 2017. How Large Igneous Provinces affect global climate,
514 sometimes cause mass extinctions, and represent natural markers in the
515 geological record. Palaeogeogr. Palaeoclimatol. Palaeoecol. 478, 30–52.
516 Fang, Q., Hong, H., Chen, Z.-Q., Yu, J., Wang, C., Yin, K., Zhao, L., Liu, Z., Cheng,
517 F., Gong, N., Furnes, H., 2017. Microbial proliferation coinciding with
518 volcanism during the Permian-Triassic transition: New, direct evidence from
519 volcanic ashes, South China. Palaeogeogr. Palaeoclimatol. Palaeoecol. 474,
520 164–186.
521 Feng, Z.Z., Jin, Z., Yang, Y., 1994. Permian Lithofacies and Paleogeography of the
522 Yunnan-Guizhou-Guangxi Regions. Geological Publishing House, Beijing.
523 Fisher, R.V., Schmincke, H.-U., 1984. Pyroclastic fragments and deposits. In: Fisher,
524 R.V., Schmincke, H.-U. (Eds), Pyroclastic Rocks. Springer, Berlin, Heidelberg,
525 pp. 89–124.

526 Flemming, H.-C., van Hullebusch, E.D., Little, B.J., Neu, T.R., Nielsen, P.H., Seviour,
527 T., Stoodley, P., Wingender, J., Wuertz, S., 2025. Microbial extracellular
528 polymeric substances in the environment, technology and medicine. Nat. Rev.
529 Microbiol. 23, 87–105.
530 Galvez, M.E., Beyssac, O., Benzerara, K., Menguy, N., Bernard, S., Cox, S.C., 2012.
531 Micro- and nano-textural evidence of Ti(–Ca–Fe) mobility during fluid ‐ rock
532 interactions in carbonaceous lawsonite-bearing rocks from New Zealand. Contrib.
533 Mineral. Petrol. 164, 895–914.
534 Gao, R., Wu, T., Kerr, A., Liu, H., Xiao, L., Huang, W., 2025. Zircon U-Pb ages and
535 Sr-Nd-Hf isotope geochemistry of I-type granites in the Jiangda-Weixi region,
536 eastern Tibet: implications for the tectonic evolution of the Paleo-Tethyan
537 orogeny. J. Earth Sci. 36(6), 2387–2410.
538 Glaub, I., Vogel, K., 2004. The stratigraphic record of microborings. Fossils and Strata
539 51, 126–135.
540 Golubic, S., Brent, G., Lecampion, T., 1970. Scanning electron microscopy of
541 endolithic algae and fungi using a multipurpose casting-embedding technique.
542 Lethaia 3, 203–209.
543 Golubic, S., Perkins, R.D., Lukas, K.J., 1975. Boring microorganisms and
544 microborings in carbonate substrates. In: Frey, R.W. (Ed.), The Study of Trace
545 Fossils: A Synthesis of Principles, Problems, and Procedures in Ichnology.
546 Springer, Berlin, Heidelberg, pp. 229–259.

547 Golubic, S., Seong-Joo, L., Browne, K.M., 2000. Cyanobacteria: Architects of
548 sedimentary structures. In: Riding, R.E., Awramik, S.M. (Eds), Microbial
549 Sediments. Springer, Berlin, Heidelberg, pp. 57–67.
550 Guo, Z., Peng, X., Czaja, A.D., Chen, S., Ta, K., 2018. Cellular taphonomy of
551 well-preserved Gaoyuzhuang microfossils: A window into the preservation of
552 ancient cyanobacteria. Precambrian Res. 304, 88–98.
553 Haq, B.U., Schutter, S.R., 2008. A chronology of Paleozoic sea-level changes. Science
554 322, 64–68.
555 He, B., Xu, Y.-G., Chung, S.-L., Xiao, L., Wang, Y., 2003. Sedimentary evidence for a
556 rapid, kilometer-scale crustal doming prior to the eruption of the Emeishan flood
557 basalts. Earth Planet. Sci. Lett. 213, 391–405.
558 He, B., Xu, Y.-G., Huang, X.-L., Luo, Z.-Y., Shi, Y.-R., Yang, Q.-J., Yu, S.-Y., 2007.
559 Age and duration of the Emeishan flood volcanism, SW China: Geochemistry
560 and SHRIMP zircon U–Pb dating of silicic ignimbrites, post-volcanic Xuanwei
561 Formation and clay tuff at the Chaotian section. Earth Planet. Sci. Lett. 255,
562 306–323.
563 Hoppe, P., Cohen, S., Meibom, A., 2013. NanoSIMS: Technical aspects and
564 applications in cosmochemistry and biological geochemistry. Geostand. Geoanal.
565 Res. 37, 111–154.
566 Huang, H., Cawood, P.A., Hou, M.-C., Yang, J.-H., Ni, S.-J., Du, Y.-S., Yan, Z.-K.,
567 Wang, J., 2016. Silicic ash beds bracket Emeishan Large Igneous province to < 1
568 m.y. at ~ 260 Ma. Lithos 264, 17–27.

569 Huang, H., Huyskens, M.H., Yin, Q.-Z., Cawood, P.A., Hou, M., Yang, J., Xiong, F.,
570 Du, Y., Yang, C., 2022. Eruptive tempo of Emeishan large igneous province,
571 southwestern China and northern Vietnam: Relations to biotic crises and
572 paleoclimate changes around the Guadalupian-Lopingian boundary. Geology 50,
573 1083–1087. https://doi.org/10.1130/G50183.1
574 Huang, Y.G., Chen, Z.-Q., Wignall, P.B., Grasby, S.E., Zhao, L.S., Wang, X.D., Kaiho,
575 K., 2019a. Biotic responses to volatile volcanism and environmental stresses
576 over the Guadalupian-Lopingian (Permian) transition. Geology 47, 175–178.
577 Huang, Y.G., Chen, Z.-Q., Zhao, L., Stanley, G.D., Yan, J., Pei, Y., Yang, W., Huang,
578 J., 2019b. Restoration of reef ecosystems following the Guadalupian-Lopingian
579 boundary mass extinction: Evidence from the Laibin area, South China.
580 Palaeogeogr. Palaeoclimatol. Palaeoecol. 519, 8–22.
581 Itamiya, H., Sugita, R., Sugai, T., 2019. Analysis of the surface microtextures and
582 morphologies of beach quartz grains in Japan and implications for provenance
583 research. Progr. Earth Planet. Sci. 6, 43.
584 Jin, Y.G., Zhang, J., Shang, Q.H., 1994a. Two phases of the end-Permian mass
585 extinction. In: Beauchamp, B., Embry, A., Glass, D. (Eds), Pangea: Global
586 Environment and Resources. Canadian Soc. Petrol. Geol. Mem. 17. 813–822.
587 Jin, Y.G., Zhu, Z.L., Mei, S.L., 1994b. The Maokouan–Lopingian boundary sequences
588 in South China. Palaeoworld 4, 138–152.

589 Jin, Y., Shen, S., Henderson, C.M., Wang, X., Wang, W., Wang, Y., Cao, C., Shang, Q.,
590 2006. The Global Stratotype Section and Point (GSSP) for the boundary between
591 the Capitanian and Wuchiapingian Stage (Permian). Episodes 29, 253–262.
592 Kaiho, K., Chen, Z.-Q., Ohashi, T., Arinobu, T., Sawada, K., Cramer, B.S., 2005. A
593 negative carbon isotope anomaly associated with the earliest Lopingian (Late
594 Permian) mass extinction. Palaeogeogr. Palaeoclimatol. Palaeoecol. 223,
595 172–180.
596 Kaiho, K., Grasby, S.E., Chen, Z.-Q., 2023. High-temperature combustion event
597 spanning the Guadalupian-Lopingian boundary terminated by soil erosion.
598 Palaeogeogr. Palaeoclimatol. Palaeoecol. 618, 111518.
599 Kawano, M., Tomita, K., 2001. Microbial biomineralization in weathered volcanic ash
600 deposit and formation of biogenic minerals by experimental incubation. Am.
601 Mineral. 86, 400–410.
602 Kołodziej, B., Golubic, S., Bucur, I.I., Radtke, G., Tribollet, A., 2012. Early
603 Cretaceous record of microboring organisms in skeletons of growing corals.
604 Lethaia 45, 34–45.
605 Langmann, B., Zakšek, K., Hort, M., Duggen, S., 2010. Volcanic ash as fertiliser for
606 the surface ocean. Atmos. Chem. Phys. 10, 3891–3899.
607 Le Campion-Alsumard, T., Golubic, S., Hutchings, P., 1995. Microbial endoliths in
608 skeletons of live and dead corals: *Porites lobata* (Moorea, French Polynesia).
609 Mar. Ecol. Progr. Ser. 117, 149–157.

Li, L., Bai, S., Li, J., Wang, S., Tang, L., Dasgupta, S., Tang, Y., Peng, X., 2020. Volcanic ash inputs enhance the deep-sea seabed metal-biogeochemical cycle: A case study in the Yap Trench, western Pacific Ocean. Mar. Geol. 430, 106340.

Li, S., Huang, Y., Chen, Z.-Q., Chen, L., Wignall, P.B., Dong, J., Liu, X., Zheng, H., Wang, G., Wei, Z., Zhu, Z., 2024. Variations in antimony isotope and toxic metals across the Guadalupian-Lopingian (Permian) boundary at Penglaitan, China: Implications for the Emeishan volcanism and marine extinction. Earth Planet. Sci. Lett. 648, 119096.

Liu, D., Chen, Z.-Q., Woods, A.D., Fang, Y., Huang, Y., Feng, X., Liu, Z., 2024. Revisiting the Yudongzi microbialites (basal Triassic, northwestern Sichuan, South China): Fabric textures and paleoenvironmental implication. Glob. Planet. Chang. 232, 104344.

Longman, J., Palmer, M.R., Gernon, T.M., Manners, H.R., Jones, M.T., 2022. Subaerial volcanism is a potentially major contributor to oceanic iron and manganese cycles. Commun. Earth. Environ. 3, 60.

Lucas, S.G., Shen, S.Z., 2018. The Permian Timescale. Geol. Soc. London, Spec. Publ. 450. https://doi.org/10.1144/SP450

Luo, M., Chen, Z.-Q., Shi, G.R., Fang, Y., Song, H., Jia, Z., Huang, Y., Yang, H., 2016. Upper Lower Triassic stromatolite from Anhui, South China: Geobiologic features and paleoenvironmental implications. Palaeogeogr. Palaeoclimatol. Palaeoecol. 452, 40–54.

631 Macintyre, I.G., Prufert-Bebout, L., Reid, R.P., 2000. The role of endolithic
632 cyanobacteria in the formation of lithified laminae in Bahamian stromatolites.
633 Sedimentology 47, 915–921.
634 Madhavaraju, J., Lee, Y.I., Armstrong-Altrin, J.S., Hussain, S.M., 2006. Microtextures
635 on detrital quartz grains of upper Maastrichtian-Danian rocks of the Cauvery
636 Basin, southeastern India: implications for provenance and depositional
637 environments. Geosci. J. 10, 23–34.
638 Maliva, R.G., Siever, R., 1988. Mechanism and controls of silicification of fossils in
639 limestones. J. Geol. 96, 387–398.
640 Mei, M., Ma, Y., Deng, J., Chu, H., Zheng, K., 2007. Sequence-stratigraphic
641 frameworks and their palaeogeographic patterns for the Permian Lopingian of
642 the Dianqiangui Basin and its adjacent areas of Southwestern China. Sci. Chin.
643 Ser. D 50, 869–885.
644 Oehler, D.Z., Robert, F., Walter, M.R., Sugitani, K., Allwood, A., Meibom, A.,
645 Mostefaoui, S., Selo, M., Thomen, A., Gibson, E.K., 2009. NanoSIMS: Insights
646 to biogenicity and syngeneity of Archaean carbonaceous structures. Precambrian
647 Res. 173, 70–78.
648 Olóriz, F., Reolid, M., Rodríguez-Tovar, F.J., 2004. Microboring and taphonomy in
649 Middle Oxfordian to lowermost Kimmeridgian (Upper Jurassic) from the
650 Prebetic Zone (southern Iberia). Palaeogeogr. Palaeoclimatol. Palaeoecol. 212,
651 181–197.

652 Pei, Y., Chen, Z.-Q., Fang, Y., Kershaw, S., Wu, S., Luo, M., 2019. Volcanism, redox
653 conditions, and microbialite growth linked with the end-Permian mass extinction:
654 Evidence from the Xiajiacao section (western Hubei Province), South China.
655 Palaeogeogr. Palaeoclimatol. Palaeoecol. 519, 194–208.
656 Peng, X., Guo, Z., House, C.H., Chen, S., Ta, K., 2016. SIMS and NanoSIMS
657 analyses of well-preserved microfossils imply oxygen-producing photosynthesis
658 in the Mesoproterozoic anoxic ocean. Chem. Geol. 441, 24–34.
659 Pernice, M., Raina, J.-B., Rädecker, N., Cárdenas, A., Pogoreutz, C., Voolstra, C.R.,
660 2020. Down to the bone: the role of overlooked endolithic microbiomes in reef
661 coral health. ISME J. 14, 325–334.
662 Perrier, V., Meidla, T., Tinn, O., Ainsaar, L., 2012. Biotic response to explosive
663 volcanism: Ostracod recovery after Ordovician ash-falls. Palaeogeogr.
664 Palaeoclimatol. Palaeoecol. 365–366, 166–183.
665 Punekar, J., Mateo, P., Keller, G., 2014. Effects of Deccan volcanism on
666 paleoenvironment and planktic foraminifera: A global survey. In: Keller, G., Kerr,
667 A.C. (Eds), Volcanism, Impacts, and Mass Extinctions: Causes and Effects.
668 Geological Society of America, pp. 91–116
669 Qiu, X., Yang, H., Zheng, Z., Fang, Q., Chen, Z.-Q., 2025. NanoSIMS techniques and
670 its important implications in Geomicrobiology and Biosedimentology. Earth Sci.
671 50(3), 1220–1233 (Chinese).
672 Racki, G., 2020. A volcanic scenario for the Frasnian-Famennian major biotic crisis
673 and other Late Devonian global changes: More answers than questions? Glob.

674 Planet. Chang. 189, 103174.
675 Radtke, G., 1991. Die mikroendolithischen Spurenfossilien im Alt-Tertiär
676 West-Europas und ihre palökologische Bedeutung. Cour. Forsch. Senckenberg
677 138, 1–185.
678 Reid, R.P., Macintyre, I.G., 2000. Microboring versus recrystallization: further insight
679 into the micritization process. J. Sediment. Res. 70, 24–28.
680 Rifl, M., Vacek, F., Holcová, K., 2022. Microboring variability in bioclasts from a
681 carbonate platform and a mixed carbonate ramp: Paleoenvironmental
682 implications (Upper Triassic, Slovenia). Mar. Micropaleontol. 170, 102077.
683 Schmitt, J.G., Boyd, D.W., 1981. Patterns of silicification in Permian pelecypods and
684 brachiopods from Wyoming. J. Sediment. Res. 51, 1297–1308.
685 Shen, S.Z., Shi, G.R., 2002. Paleobiogeographical extinction patterns of Permian
686 brachiopods in the Asian-western Pacific region. Paleobiology 28, 449–463.
687 Shen, S.Z., Wang, Y., Henderson, C.M., Cao, C.Q., Wang, W., 2007. Biostratigraphy
688 and lithofacies of the Permian system in the Laibin-Heshan area of Guangxi,
689 South China. Palaeoworld 16, 120–139
690 Shen, S., Yuan, D., Zhang, Y., Charles, M.H., Zheng, Q., Zhang, H., Zhang, M., Dai,
691 Y., Xu, H., Wang, W., Li, Q., Wang, Y., Wang, X., Mu, L., Ramezani, J., Erwin,
692 D.H., Angiolini, L., Zhang, F., Hou, Z., Chen, J., Zhang, X., Zhang, S., Wu, Q.,
693 Pan, Y., Stephenson, M., Mei, S., 2023. Redefinition of the Global Stratotype
694 Section and Point (GSSP) and new Standard Auxiliary Boundary Stratotype
695 (SABS) for the base of Wuchiapingian Stage (Lopingian Series, Permian) in

696 South China. Episodes 47, 147–177.
697 Sirantoine, E., Wacey, D., Bischoff, K., Saunders, M., 2021. Authigenic anatase
698 within 1 billion-year-old cells. Geobiology 19, e12417.
699 Smyth, H.R., Hall, R., Nichols, G.J., 2008. Significant volcanic contribution to some
700 quartz-rich sandstones, East Java, Indonesia. J. Sediment. Res. 78, 335–356.
701 Song, H., Algeo, T.J., Song, H., Tong, J., Wignall, P.B., Bond, D.P.G., Zheng, W.,
702 Chen, X., Romaniello, S., Wei, H., Anbar, A.D., Global oceanic anoxia linked
703 with the Capitanian (Middle Permian) marine mass extinction. Earth Planet. Sci.
704 Lett. 610, 118128.
705 Stanley, S.M., Yang, X.L., 1994. A double mass extinction at the end of the Paleozoic
706 era. Science 266, 1340–1344.
707 Sun, Y., Lai, X., Wignall, P.B., Widdowson, M., Ali, J.R., Jiang, H., Wang, W., Yan, C.,
708 Bond, D.P.G., Védrine, S., 2010. Dating the onset and nature of the Middle
709 Permian Emeishan large igneous province eruptions in SW China using
710 conodont biostratigraphy and its bearing on mantle plume uplift models. Lithos
711 119, 20–33
712 Svensen, H., Planke, S., Polozov, A.G., Schmidbauer, N., Corfu, F., Podladchikov,
713 Y.Y., Jamtveit, B., 2009. Siberian gas venting and the end-Permian
714 environmental crisis. Earth Planet. Sci. Lett. 277, 490–500.
715 Trembath-Reichert, E., Shah Walter, S.R., Ortiz, M.A.F., Carter, P.D., Girguis, P.R.,
716 Huber, J.A., 2021. Multiple carbon incorporation strategies support microbial
717 survival in cold subseafloor crustal fluids. Sci. Adv. 7, eabg0153.

718 Wacey, D., Kilburn, M.R., Saunders, M., Cliff, J., Brasier, M.D., 2011. Microfossils of
719 sulphur-metabolizing cells in 3.4-billion-year-old rocks of Western Australia. Nat.
720 Geosci. 4, 698–702.
721 Wang, W., Cao, C.Q., Wang, Y., 2004. The carbon isotope excursion on GSSP
722 candidate section of Lopingian–Guadalupian boundary. Earth Planet. Sci. Lett.
723 220, 57–67.
724 Wang, Y., Jin, Y.G., 2000. Permian palaeogeographic evolution of the Jiangnan Basin,
725 South China. Palaeogeogr. Palaeoclimatol. Palaeoecol. 160, 35–44.
726 Waśkowska, A., 2011. Response of Early Eocene deep-water benthic foraminifera to
727 volcanic ash falls in the Polish Outer Carpathians: Palaeocological implications.
728 Palaeogeogr. Palaeoclimatol. Palaeoecol. 305, 50–64.
729 Weibel, R., Friis, H., 2004. Opaque minerals as keys for distinguishing oxidising and
730 reducing diagenetic conditions in the Lower Triassic Bunter Sandstone, North
731 German Basin. Sediment. Geol. 169, 129–149.
732 Werne, J.P., Hollander, D.J., Behrens, A., Schaeffer, P., Albrecht, P., Sinninghe
733 Damsté, J.S., 2000. Timing of early diagenetic sulfurization of organic matter: a
734 precursor-product relationship in Holocene sediments of the anoxic Cariaco
735 Basin, Venezuela. Geochim. Cosmochim. Acta 64, 1741–1751.
736 Wignall, P.B., Védrine, S., Bond, D.P.G., Wang, W., Lai, X.-L., Ali, J.R., Jiang, H.-S.,
737 2009. Facies analysis and sea-level change at the Guadalupian–Lopingian Global
738 Stratotype (Laibin, South China), and its bearing on the end-Guadalupian mass
739 extinction. J. Geol. Soc. 166, 655–666.

740 Win, S., Feng, Q., Swe, Y.M., Zhao, T., Gan, Z., Nie, X., Khaing, A., Aung, S.N.L.,
741 2025. Early Carboniferous magmatic rocks in eastern Myanmar: implications for
742 the Tethyan evolution. J. Earth Sci. 36(6), 2450–2464.
743 Wisshak, M., Seunß, B., Nützel, A., 2008. Evolutionary implications of an
744 exceptionally preserved Carboniferous microboring assemblage in the Buckhorn
745 Asphalt lagerstätte (Oklahoma, USA). In: Wisshak, M., Tapanila, L. (Eds),
746 Current Developments in Bioerosion, Erlangen Earth Conference Series.
747 Springer, Berlin, Heidelberg, pp. 21–54.
748 Wisshak, M., 2012. Chapter 8 – Microbioerosion. In: Knaust, D., Bromley, R.G. (Eds),
749 Developments in Sedimentology, Trace Fossils as Indicators of Sedimentary
750 Environments. Elsevier, pp. 213–243.
751 Wu, S., Chen, Z.-Q., Fang, Y., Pei, Y., Yang, H., Ogg, J., 2017. A Permian-Triassic
752 boundary microbialite deposit from the eastern Yangtze Platform (Jiangxi
753 Province, South China): Geobiologic features, ecosystem composition and redox
754 conditions. Palaeogeogr. Palaeoclimatol. Palaeoecol. 486, 58–73.
755 Wu, Y.B., Feng, Q., Gong, Y.M., 2013. Blooming of bacteria and algae is a biokiller
756 for mass-extinction of Devonian coral-stromatoporoid reef ecosystems. Science
757 China: Earth Sci. 43, 1156–1167.
758 Xiao, D., Huang, T., Xu, Q., Tan, X., Wen, L., Zheng, J., Cao, J., 2024. Two pulsed
759 activities of the Emeishan large igneous province in southwestern China inferred
760 from dolomite U-Pb geochronology and significance. Geol. Soc. Am. Bull. 136,
761 3977–3992.

762 Xu, Y.-G., He, B., Chung, S.-L., Menzies, M.A., Frey, F.A., 2004. Geologic,
763 geochemical, and geophysical consequences of plume involvement in the
764 Emeishan flood-basalt province. Geology 32, 917–920.
765 Zhang, B., Wignall, P.B., Yao, S., Hu, W., Liu, B., 2021. Collapsed upwelling and
766 intensified euxinia in response to climate warming during the Capitanian (Middle
767 Permian) mass extinction. Gondwana Res. 89, 31–46.
768 Zhang, R., Jiang, T., Tian, Y., Xie, S., Zhou, L., Li, Q., Jiao, N., 2017. Volcanic ash
769 stimulates growth of marine autotrophic and heterotrophic microorganisms.
770 Geology 45, 679–682.
771 Zhao, X., Liu, R., Wang, F., Li, Q., Su, C., Ding, J., Xiong, C., Li, W., Zhang, J., Hou,
772 K., 2025. Determining the age of Guadalupian extinction by in situ uranium–lead
773 geochronology in regard to middle Permian giant bivalve Alatoconchidae fossils
774 in the Northwest margin of the South China Plate. Gondwana Research 150,
775 405–418. https://doi.org/10.1016/j.gr.2025.10.008
776 Zhong, Y.-T., He, B., Xu, Y.-G., 2013. Mineralogy and geochemistry of claystones
777 from the Guadalupian–Lopingian boundary at Penglaitan, South China: Insights
778 into the pre-Lopingian geological events. J. Asian Earth Sci. 62, 438–462.
779 Ziegler, A.M., Gibbs, M.T., Hulver, M.L., 1998. A mini-atlas of oceanic water masses
780 in the Permian period. Trans. Roy. Soc. Victoria 110, 323–343.
781

Figures and figure captions

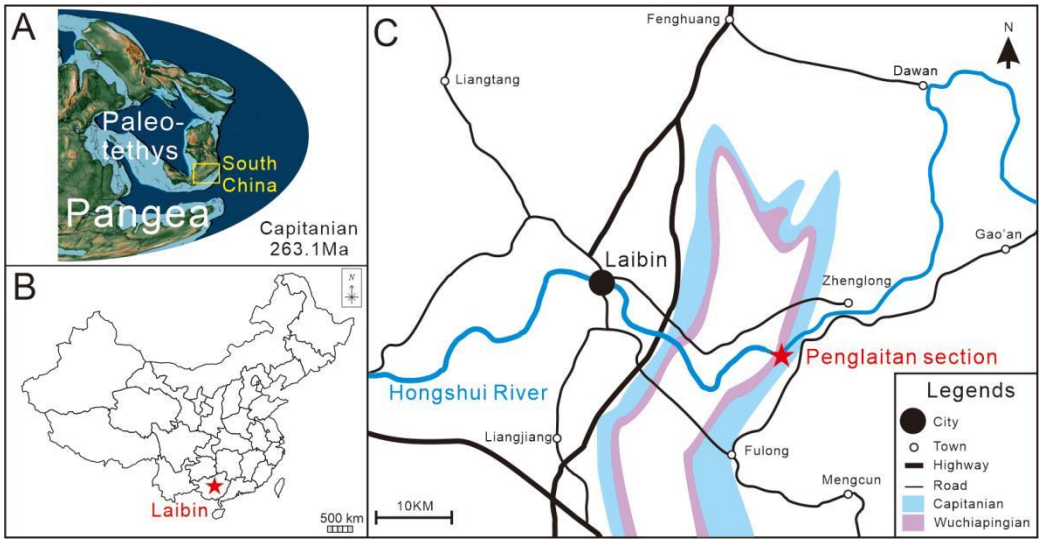

Fig. 1. Middle Permian global paleogeographic map (A; modified from Ziegler et al., 1998) showing the location of South China, and modern geographic map (B) showing the location of Laibin area. Geographic map (C) showing locality of the Penglaitan section (modified from Jin et al., 2006).

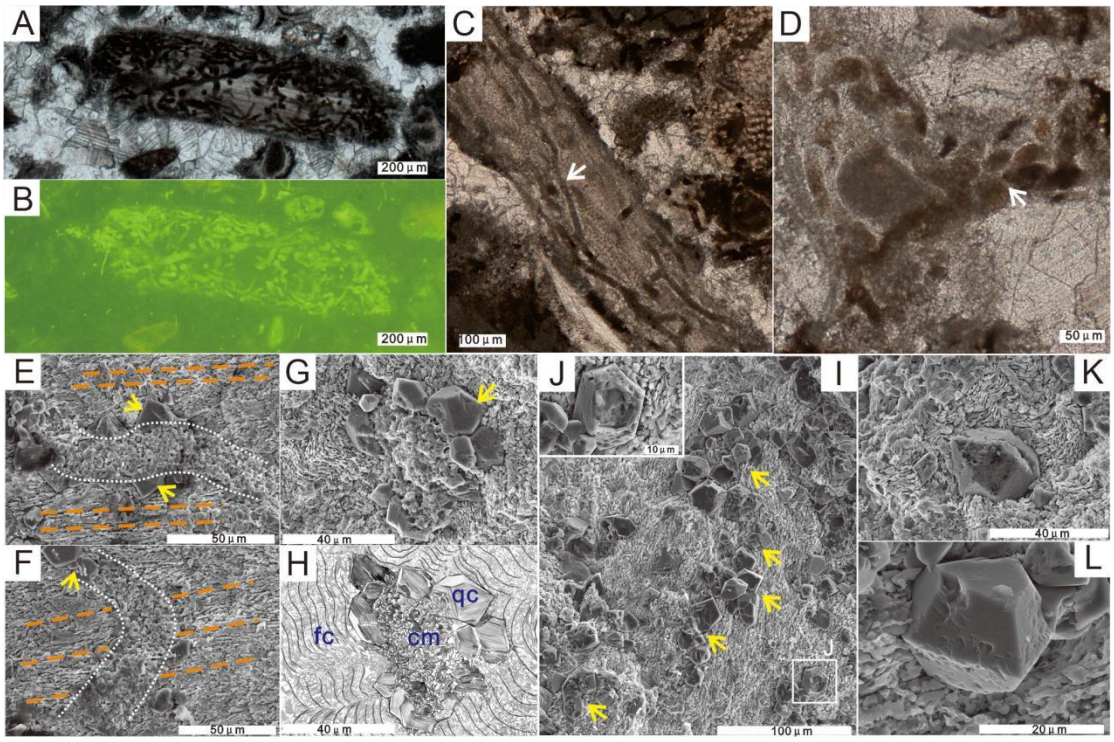

792

793 **Fig. 2.** Selected microphotographs of thin sections (A–D), and SEM images (E–L) of

794 microborings and quartz crystals from the Penglaitan section. (A–B) Nodular

795 microborings in brachiopod shell (A) with strong fluorescence (B). (C–D)

796 Filamentous and radial microborings (white arrows) in brachiopod shell and bryozoan

797 skeleton, respectively. (E–F) Microborings embedded parallel (E) and perpendicular

798 (F) to fibrous layers of brachiopod shell under SEM, with clay minerals filling

799 microboring and quartz crystals (yellow arrows) along microboring margins (white

800 dot lines). Yellow dash lines indicate directions of fibrous layers (E, F). (G–H) Cross

801 section of a microboring and its sketch (H) showing that a microboring truncates

802 fibrous calcite (fc) layers of brachiopod shell, with quartz crystals (qc) along

803 microboring margin and clay minerals (cm) in its center. (I–L) SEM images showing

804 quartz crystals embedded in the outer layers near the surface of the non-boring part of

805 the same brachiopod shell. (I–J) A large number of quartz crystals (yellow arrows),

oriented differently from the texture of the fibrous shell, are distributed across its surface, which also shows indentations (J). (K) A hexagonal quartz crystal embedded within the fibrous shell. (L) The tetrahedral-shaped quartz crystal.

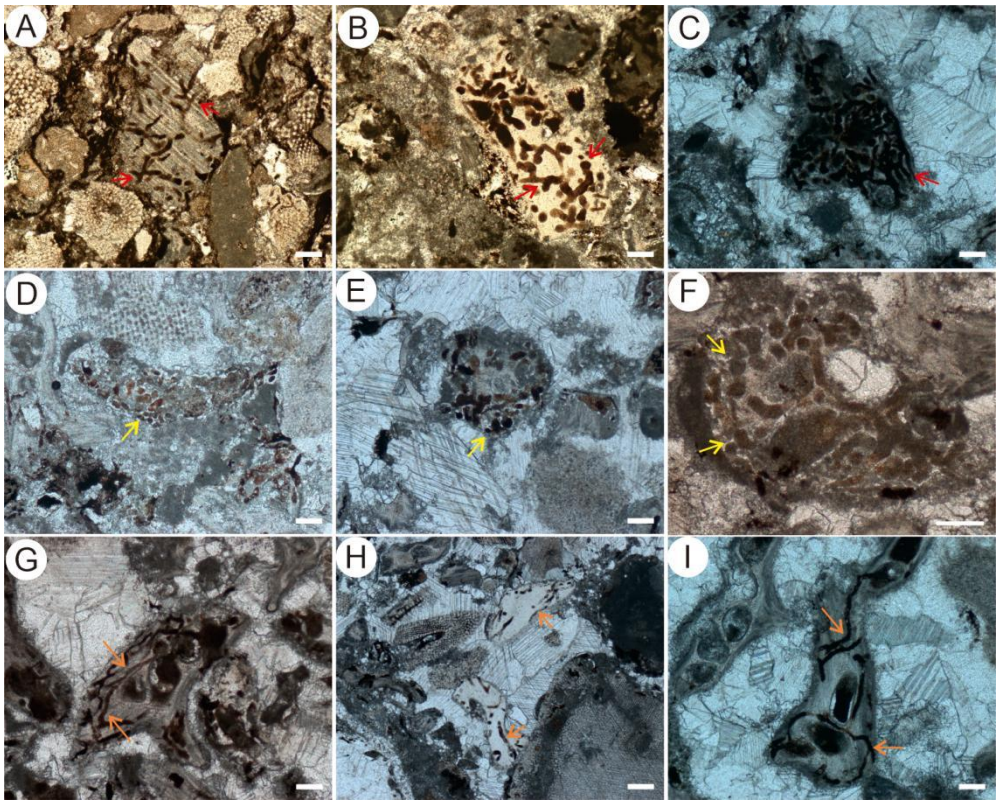

Fig. 3. Various morphologies of additional microborings from the upper Laibin Limestone of the Maokou Formation at the Penglaitan section, South China. (A–C) Nodular, strip-shaped microborings, with nodular appendices (red arrows in Fig. 3B). (D–F) Radial microborings (yellow arrows). (G–I) Filamentous microborings (orange arrows). Scale bar = 100 μm.

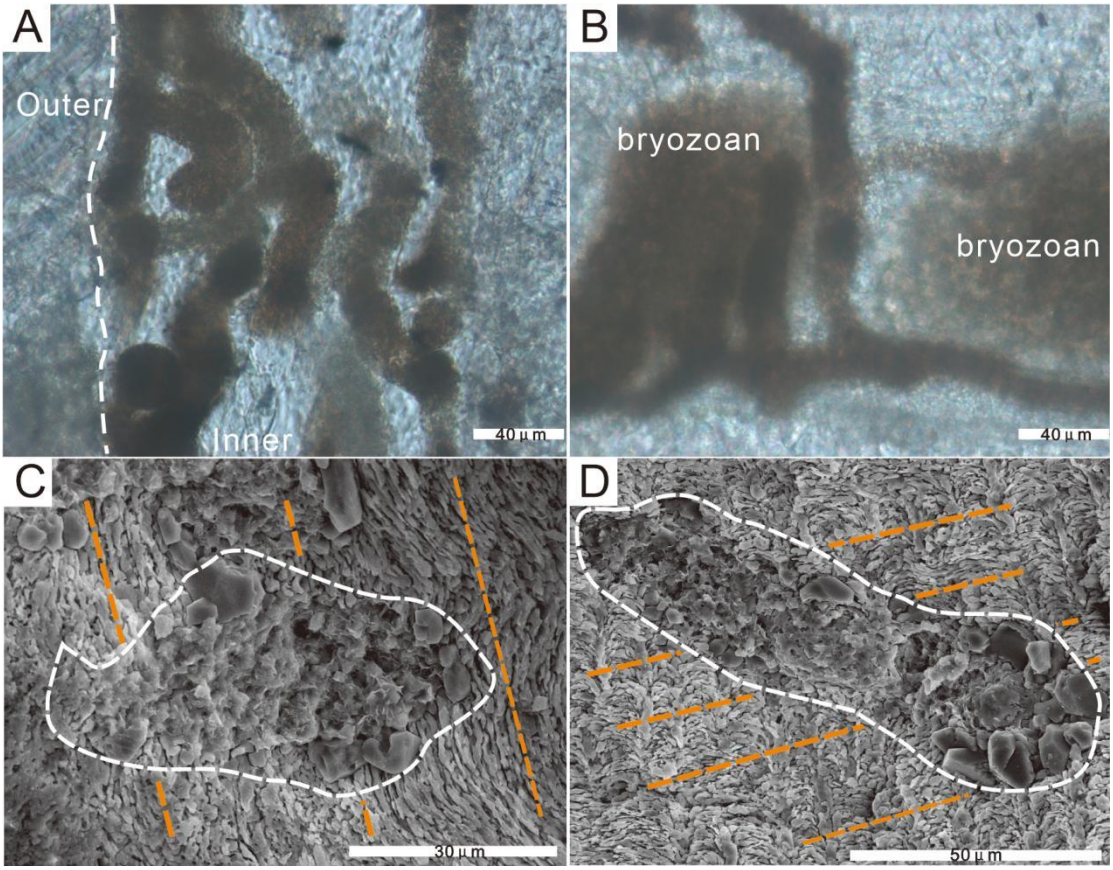

817

818 **Fig. 4.** Microphotographs (A and B) and SEM images (C and D) of additional

819 microborings details. (A–B) Microborings are well-preserved within bioclasts with

820 micrite, without inner significant recrystallization. (C–D) Microborings disrupt

821 texture of fibrous shell and are filled with clay minerals. White dash lines indicate

822 outlines of microborings, while orange dash lines represent the extending directions of

823 shell texture.

824

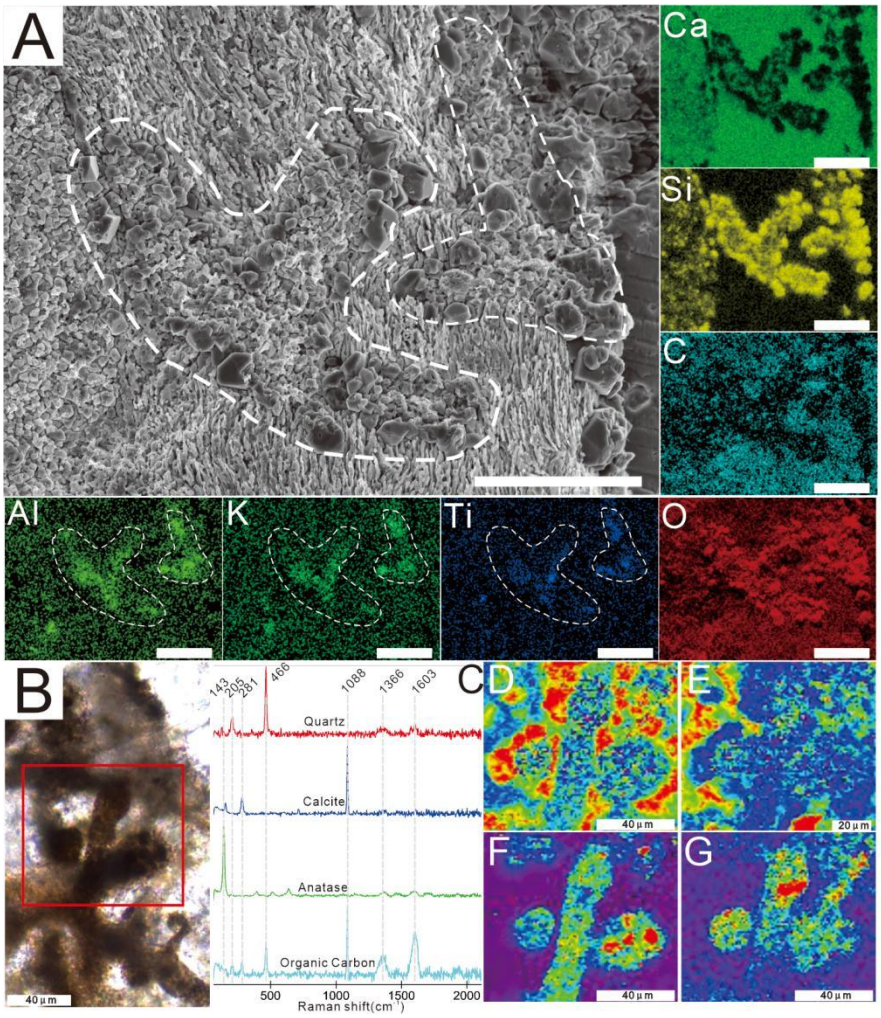

825

826 **Fig. 5.** SEM image and EDS mappings (A) and Raman spectrum analyses of

827 microborings (B–G). (A) two microborings on a brachiopod shell and elemental

828 distributions in fillings; note that abundant quartz crystals are distributed along

829 microboring margins; elements Si, Al, K, Ti and O are enriched in microboring, while

830 Ca and C are enriched in hosting shell. (B–C) Microphotograph of nodular

831 microborings (B) and Raman spectrum peaks of quartz (~466 cm^{-1}), calcite (~281 and

832 1088 cm^{-1}), anatase (~143, 395, 517, 638 cm^{-1}) and organic carbon (~1366 cm^{-1} and

833 ~1603 cm^{-1}) in microboring filling (C). (D–G) Raman spectrum mappings showing

834 that distributions of quartz (466 cm^{-1}; D), calcite (1088 cm^{-1}; E), anatase (143 cm^{-1}; F)

835 and organic carbon (1603 cm^{-1}; G) in microboring. The brighter color represents the

836 higher content of ingredient.

837

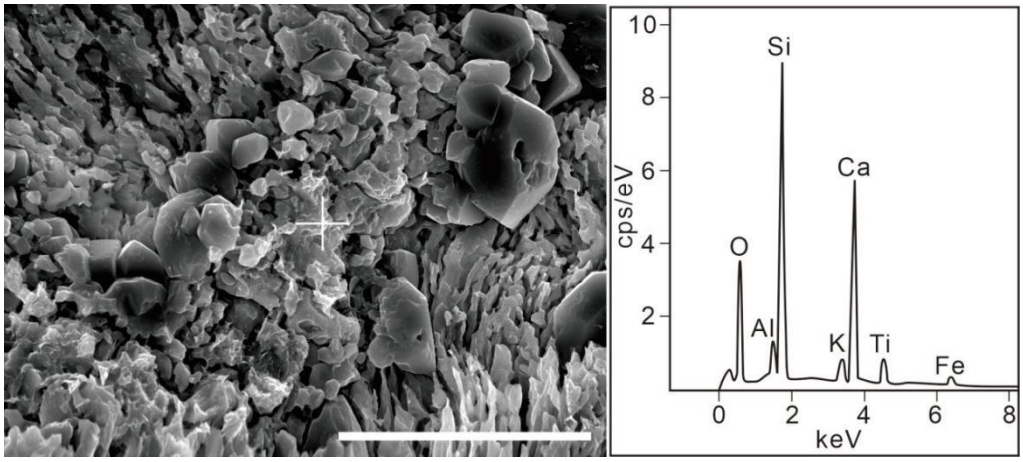

838

839 **Fig. 6.** EDS point analysis reveals elemental compositions of microboring fills: Si, Ca

840 and O are most abundant, while Al, K, Ti and Fe are moderate. The location of

841 analysis is selected from Fig. 5A. Scale bar = 30 μm.

842

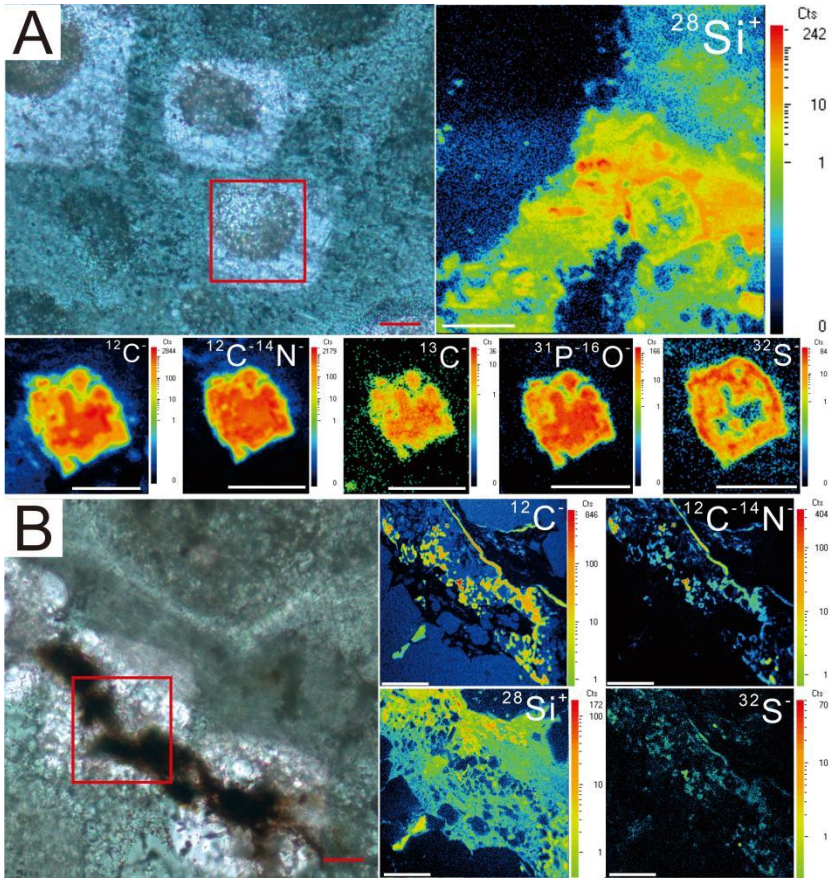

843

844 **Fig. 7.** NanoSIMS ion maps of microborings in cross section (A) and longitudinal
845 view (B). (A) Microphotograph of a microboring in cross section and NanoSIMS ion
846 maps showing stronger ion signal of $^{28}Si^{+}$ and $^{32}S^{-}$ along microboring margins, while
847 $^{12}C^{-}$, $^{12}C^{14}N^{-}$, and P are rather high within fills. (B) Microphotograph of a microboring
848 in longitudinal section and NanoSIMS ion maps showing stronger in signals of $^{12}C^{-}$
849 and $^{12}C^{14}N^{-}$ in fills, and strong signals of $^{28}Si^{+}$ around microboring margins. Scale bar
850 = 10 μm (white) and 20 μm (red).

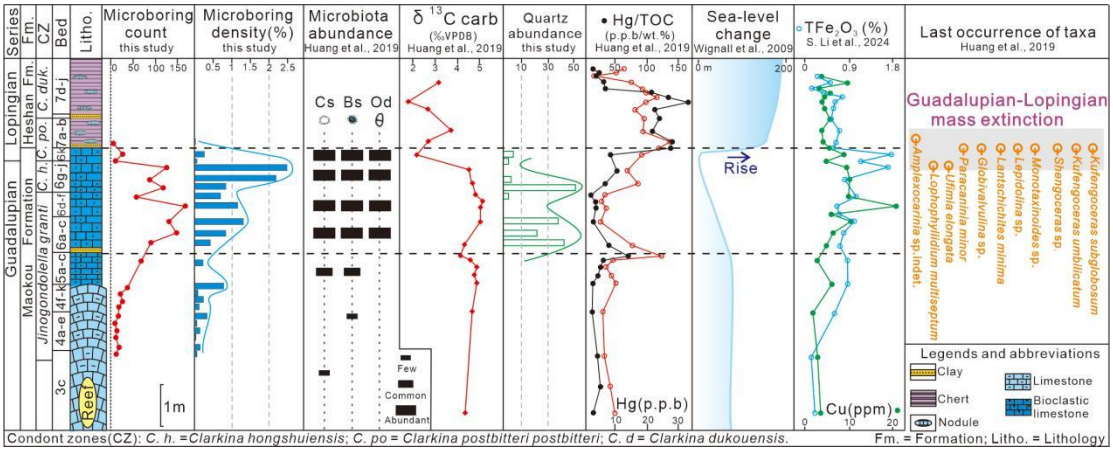

851

852 **Fig. 8.** Composite correlations of stratigraphic abundance of microborings, microbiota
853 and quartz grains with $\delta^{13}C_{carb}$ and Hg/TOC excursions, sea-level change, TFe_2O_3, Cu
854 and last occurrence of taxa through the G–L transition in the Penglaitan section.
855 Microbiota: coccoid-like spheroids (Cs), bacterial clump-like spheroids (Bs) and
856 *Ovummurus duoportius* (Od). Detailed of microboring counts, microboring density and
857 stratigraphic abundance of quartz grains/crystals are available in Supplementary Table
858 S1, Table S2 and Table S3, respectively.
859